

MAPPING THE CMB II: THE SECOND FLIGHT OF THE QMAP EXPERIMENT

T. HERBIG^{1,4}, A. DE OLIVEIRA-COSTA^{1,2}, M. J. DEVLIN³, A. D. MILLER¹, L. PAGE¹, AND
M. TEGMARK^{2,4}

Submitted to Astrophysical Journal Letters August 5, 1998

ABSTRACT

We report the results from the second flight of *QMAP*, an experiment to map the cosmic microwave background near the North Celestial Pole. We present maps of the sky at 31 and 42 GHz as well as a measurement of the angular power spectrum covering $40 \lesssim \ell \lesssim 200$. Anisotropy is detected at $\gtrsim 20\sigma$ and is in agreement with previous results at these angular scales. We also report details of the data reduction and analysis techniques which were used for both flights of *QMAP*.

Subject headings: cosmic microwave background—cosmology: observations

1. INTRODUCTION

The *QMAP* experiment is a balloon-borne telescope designed to map the cosmic microwave background (CMB) from angular scales of 0.7 to several degrees. Its design is similar to that of the Saskatoon experiment (Wollack et al. 1997), but the absence of significant atmospheric emission at balloon altitudes and the interlocking scan pattern allow the production of a sky map in an area close to the North Celestial Pole (NCP). *QMAP* flew twice in 1996.

The telescope has 6 radiometry channels in 3 dual-polarization beams. Two of these channels are at Ka-band (31 GHz) and four are at Q-band (42 GHz). The telescope can be pointed in azimuth, but the beams have a fixed elevation of about 41° . The three beams are chopped sinusoidally in azimuth at 4.6 Hz over an angle of up to $\theta_c = 20^\circ$ on the sky. In addition, the azimuth of the telescope is “wobbled” sinusoidally with periods of 50–100 s and amplitudes of approximately half the chop amplitude.

This *Letter* reports the results from the second flight of *QMAP*. It also details the calibration and pointing analysis common to both flights of the experiment. A companion paper (Devlin et al. 1998, hereafter D98) presents the results of flight 1 and discusses the design and performance of the instrument. Another companion paper (de Oliveira-Costa et al. 1998; dO98) presents the combined results from both flights and explains the mapping technique and the method used to calculate the angular power spectrum of the CMB.

2. OBSERVATIONS AND DATA

The second flight of the *QMAP* experiment was launched 1996 November 10 at 23:05 UT from Ft. Sumner, NM, by the National Scientific Balloon Facility (NSBF). The gondola reached its float altitude of 30 km two hours later and stayed at float until 12:55 UT. Science and calibration data were taken between 01:00 and 12:10 UT, all during the night. The flight was terminated 350 km east, near Shamrock, TX.

¹Princeton University, Physics Department, Jadwin Hall, Princeton, NJ 08544; herbig@puppp.princeton.edu

²Institute for Advanced Study, Olden Lane, Princeton, NJ 08540

³University of Pennsylvania, Department of Physics and Astronomy, David Rittenhouse Lab., Philadelphia, PA 19104

⁴Hubble Fellow

In contrast to flight 1, this flight was optimized for a higher signal/noise ratio for each map pixel; this was achieved with a smaller chop of $\theta_c = 5^\circ$ and a wobble of $\Delta az \approx 3^\circ$ at a period of 50 s. Because the latitude of the flight was $\approx 3^\circ$ higher than flight 1, the resulting maps are closer to the NCP. The sky coverage for both flights is shown in D98. The target region around the NCP was observed in 3 segments of 17305 s, 9200 s, and 3974 s duration, interrupted by celestial calibrations. At the chop frequency of 4.6 Hz and the data rate of 160 samples/chop, 22,433,920 radiometry samples on the NCP were gathered in each channel. All 6 channels functioned cleanly—no data had to be excised because of excess noise.

During ascent, the attitude computer froze repeatedly, which delayed starting the radiometer cooling system and prevented the radiometer from reaching thermal equilibrium. The resulting amplifier gain variations were tracked and corrected using periodic calibration pulses. Also during ascent, the data acquisition computer froze for ≈ 50 s but resumed functioning without rebooting. Consequently, the data buffers overflowed, resulting in large timing offsets between radiometry, chopper, and pointing samples. This complicated the phase solutions described in section 3.2. No other timing delays were encountered.

The primary CCD pointing camera had an 8° field of view, while the secondary camera covered 12° ; both guided with $< 10''$ intrinsic pointing noise at 10 Hz. Almost all observations were made using the narrow-field camera. As discussed in section 3.1, no stars were observed in the CCD during the radiometer calibration on Cas A, resulting in a large azimuth pointing uncertainty. Two ballast drops during the second NCP segment, tracked well in the pointing, had no discernible effect on the data.

Apart from the radiometer, all system components reached thermal regulation quickly. Exposed passive elements, such as the chopper and the mirror, cooled to temperatures of ≈ -45 C upon reaching float altitude, and stayed within 10 K for the remainder of the flight. The gondola position was recorded every minute by the GPS receivers in the NSBF flight package; time was recorded to 2 s absolute accuracy with the on-board clock.

3. ANALYSIS

The analysis procedure is similar for both flights of *QMAP*; the key differences are a degraded CCD focus in

flight 1 and large phase delays in flight 2.

3.1. Pointing

For both flights, the CCD camera was the primary pointing device. For each second of data, the az/el positions of the guide stars and planets were calculated using the on-board clock and the GPS position of the telescope. The camera scale was calibrated by measuring the positions of several stars visible in the camera field while the telescope was held at constant azimuth using the magnetometer. From laboratory measurements of the chopper and camera orientations and our limits on the camera horizon during flight, we find that the maximum deviation of the beam at the endpoints of the maximum chop ($\theta_c = 20^\circ$) is < 0.1 in elevation.

The offset of the CCD center from the radio beams was determined directly in flight 1, where a guide star was available while the radio source Cas A was observed. During flight 2, no guide star was found (Cas A was setting instead of rising), and the radio center (at $az = -39^\circ$) had to be transferred to the CCD center (at the NCP) using the magnetometer. The magnetometer was calibrated using CCD star positions at various azimuths ($-0.8 < az < +138.1$, which excludes the azimuth of Cas A) and a global fit during a full spin of the telescope. From this, we estimate the remaining uncertainty in the radio positions at 0.5 in azimuth, or 0.4 on the sky. The resulting smearing of map pixels is minor: depending on the channel, the average smearing is 0.06 , with only 10% of Ka1/2 and Q1/2 samples smeared by more than 0.12 (0.19 for Q3/4). No section of the map is smeared more than 0.2 (0.3 for Q3/4), small compared to the beam sizes.

The pointing analysis of flight 1 was complicated by a defocused CCD camera, which resulted in $5'$ pointing noise at 10 Hz as well as distortions of the CCD camera field of ≈ 0.5 at the edges. The pointing noise could be smoothed easily, while the field distortions caused the azimuth wobble to appear as elevation nodding at the wobble frequency and its first harmonic. From observations of Cas A we found this nodding to be spurious and suppressed it for subsequent analysis.

Additional pointing effects include elevation drifts at $\tau \sim 300$ s of $\Delta el \sim 0.1$ and 0.4 for flights 1 and 2, respectively, which are likely caused by altitude changes of the balloon. In addition, pendulation modes (primarily at 15 s) were excited on occasion to amplitudes of 0.1 – 0.2 , with damping times of 10 min to half amplitude. All of these modes were tracked with the camera in azimuth and elevation and are included in the pointing solution. Their effect on telescope roll is of second order and could not be tracked.

3.2. Phases

The QMAP data set consists of three parallel data streams: radiometry data, chopper position, and CCD star position. The optimum phases to associate a radiometry sample with a chopper and a pointing position are determined by maximizing the signal from Cas A with a two-dimensional search in relative phase of the radiometry to both the chopper and the pointing. The two levels of pointing modulation (chop and wobble) are essential to breaking the 180° degeneracy encountered with one modulation only.

The phase fits for flight 2 were more complicated than those for flight 1 because of the buffer overflows described above. While the flight 1 chopper-to-pointing lag was 66 ms and the data-to-chopper lag was 46–48 ms, the corresponding lags for flight 2 were 12.17 s and 19.34–19.40 s, respectively. Despite being large, these phases are accurate to one chopper cycle for pointing and to 0.08 samples (0.1 ms) for the data, indicating that there is no significant phase smearing in either flight. The calibration pulses gave an independent check of the phase solutions in both flights.

3.3. Gain Drift Correction

As described in D98, we inject calibration pulses of constant strength and roughly 40 samples duration into each radiometry channel before the first amplifier, allowing us to monitor the total gain of each channel throughout the flight. The pulses reveal that in both flights the instrument gain drifted smoothly by about 10–15% in each channel. These drifts were modeled and applied as corrections in the subsequent analysis. The corrected gains vary $< 1\%$ throughout the flight.

3.4. Radiometry Offsets

The chop-synchronous radiometry offset was determined during mapmaking as described in dO98. This offset is produced by the variation in effective emissivity of the chopper plate (Wollack et al. 1997) and by the modulation of emissive cavities in the optical layout. In the mapping analysis, the radiometry offset was calculated over one chopper cycle without regard to the actual chopper position. When the results are folded by chopper deflection, the offsets at overlapping positions are in agreement, as illustrated in Figure 1 for the Ka1 channel. This validates both the phasing and the radiometry offset analysis.

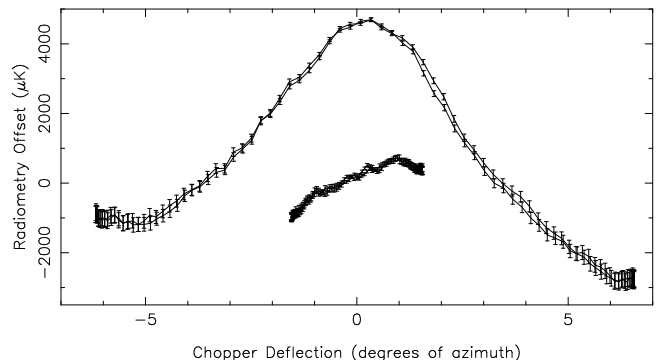


FIG. 1.— Chop-synchronous radiometry offset for channel Ka1 from flight 1 (wide curve) and flight 2 (narrow curve) as a function of chopper deflection. Note the agreement of the folded curves, which is similar in the other channels.

3.5. Beams

The beam patterns were measured as part of our system calibration, with $\theta_c = 3^\circ$ and $\Delta az = 5^\circ$ in flight 1 and 1.4° in flight 2. Because the elevation of the beams is fixed, the vertical component of the beam map is obtained by a drift scan.

The beam maps were calculated by gridding the raw data into 0.1 pixels. For flight 1, the chop-synchronous radiometry offset discussed in section 3.4 was subtracted directly from each channel, flattening the map background

by more than a factor of 10. In flight 2, the chop amplitude for CMB observations was smaller than that used for Cas A, so that the radiometry offset could not be subtracted from the beam maps. Figure 2 shows two beam images from flight 1. The maps for flight 2 are similar, except for slightly larger background variations.

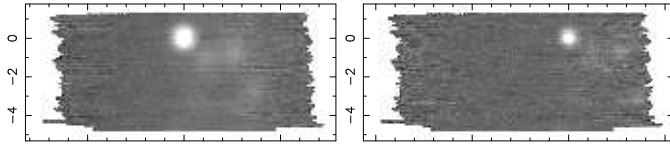


FIG. 2.— Flight 1 beam images¹⁰ of Cas A from the combined Ka1/2 channels (left) Q1/2 channels (right). The chop-synchronous radiometry offset was subtracted. The grey-scale values stretch linearly from -10 to $+15$ mK, and the axes are relative elevation and azimuth in degrees on the sky. The structure to the bottom right of Cas A corresponds to radio sources in the Galaxy.

For the beam shape determination, corresponding pairs of beams (both polarizations for each feed, *e.g.*, Ka1/2) were combined and fitted as elliptical Gaussians. The five shape parameters (*az/el* position, major and minor FWHM, and angle) for the combined beams were then used as constraints for the peak fits in each individual channel. The beam sizes are $0^{\circ}89 \pm 0^{\circ}03$, $0^{\circ}66 \pm 0^{\circ}02$ and $0^{\circ}70 \pm 0^{\circ}02$ for Ka1/2, Q1/2 and Q3/4, respectively. The robustness of these fits was explored by varying the fit window size and the background subtraction model. The resulting systematic error estimates in the beam integrals (≈ 4 – 8%) exceed the formal errors on the fit parameters and have been included in the overall calibration errors.

Our susceptibility to errors in the beam sizes is small: for the calibration, only the error in the beam integral is relevant. With our mapping approach, errors in the beam size only affect the highest multipoles of the angular power spectrum, as discussed in dO98. The beam parameters were measured independently for each flight and are in good agreement.

3.6. Calibration

Our primary calibration source is the supernova remnant Cas A, unresolved at our beam sizes, for which we used the flux densities compiled by Baars et al. (1977) augmented by data points between 31 and 250 GHz (Leitch 1998, Chini et al. 1984, Mezger et al. 1986). The resulting spectrum fit is $\log(S_{\nu}/Jy) = (5.713 \pm 0.023) - (0.759 \pm 0.006) \log(\nu/\text{MHz})$ at epoch 1980.0. We use the secular decrease model from Baars et al. (1977) to predict the flux density at our observing epochs. The uncertainty in the flux density of Cas A is approximately 8.7% (including the uncertainty in our center frequencies of ≈ 0.4 GHz) and is the largest single contributor to the overall calibration uncertainty.

Using the beam fits described in section 3.5, we predict an antenna temperature for Cas A between 15 and 25 mK, depending on band and channel. Each flight is calibrated independently.

Note that the beams used for the calibration were observed with the same strategy as the CMB data; this means that most stable systematic errors that could lead to defocussing (*e.g.*, pointing noise and drifts, pendulation, phases, and CCD camera and chopper calibrations)

¹At the highest ℓ , the fraction of the calibration error due to uncertainty in the beam is partially offset by a change in the window function. To be conservative, we do not include this effect

are automatically corrected to the appropriate calibration.

The total calibration uncertainties are between 10% and 13%, depending on channel and flight. Roughly equal amounts are uncorrelated (beam fit and center frequency) and correlated (Cas A) between channels.

3.7. Data Rejection

A small portion of the data (7.8% and 4.0% for flights 1 and 2, respectively) were rejected from the analysis. The bulk (4.8% and 4.0%) were cut around the calibration pulses (every 100 s) to allow recovery of the AC-coupled radiometer baseline. Smaller cut windows resulted in a time-dependent radiometry offset, while larger windows affected neither the radiometry offset nor the final results. The remaining rejections were due to pointing glitches (0.7% and 0.02%) and to lost guide stars (2.3% in flight 1). Apart from removing Q1 of flight 1 from analysis (see D98), there were no cuts based on the contents or quality of the radiometry data themselves.

4. RESULTS AND DISCUSSION

The techniques for producing sky maps and determining the angular power spectrum are described in detail in dO98. The mapmaking step filters the data at the fundamental and the first harmonic of the chop frequency to remove the chop-synchronous offset and pre-whitens the time power spectrum to minimize the noise correlation between samples. The map is then derived from the linear inversion of a highly over-determined system of equations involving the filtered data points and their corresponding sky pixels and residual scan-synchronous offsets. The final map product consists of a vector \mathbf{x} of N pixels (each with some position on the sky) and its $N \times N$ noise covariance matrix Σ .



FIG. 3.— Wiener-filtered maps from flight 2. The combined Ka-band map (left), the combined Q-band map (middle) and the combined map from all channels (right) are shown with the NCP is at the center of the arcs and $ra=0$ at the top, increasing clockwise. The rightmost map subtends $15^{\circ} \times 16^{\circ}$. These data are independent of those in D98.

For visualization, Figure 3 shows the Wiener-filtered versions of the maps ($\mathbf{x}_w \equiv \mathbf{S}[\mathbf{S} + \Sigma]^{-1}\mathbf{x}$), where \mathbf{S} is the covariance matrix due to the observed level of sky fluctuations. Such filtering accentuates the statistically significant features of a map.

The angular power spectrum of the sky in Figure 4 is produced directly from the combined unfiltered map in each band by expanding in signal-to-noise eigenmodes and sorting by decreasing signal-to-noise ratio. Ranges of eigenmodes are averaged to produce the points shown in Figure 4 and listed in Table 1. They do not contain the calibration error of 12% for Ka and 11% for Q¹; this er-

ror is systematic and is correlated between the bands of QMAP as well as the Saskatoon results (Netterfield et al. 1997).

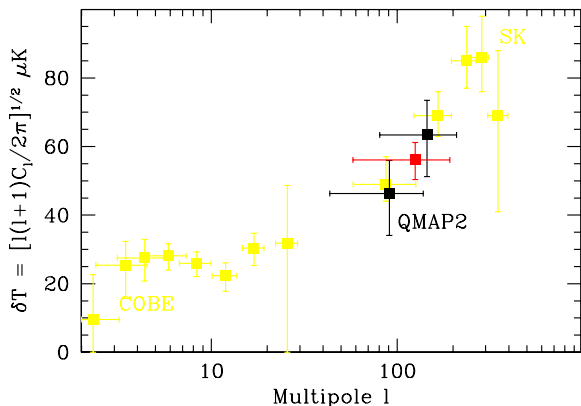


FIG. 4.— Angular power spectrum from flight 2. The central QMAP point represents Q-band. The other two represent Ka-band and have uncorrelated errors. The error bars include sample variance, but not the calibration error. For comparison, we show the results from COBE and Saskatoon (see Tegmark 1996).

Checks for systematic errors can be made by differencing the maps of each polarization pair, which cover the same sky pixels because they use the same feed. We use a generalized χ^2 statistic (dO98) to measure the signal-to-noise ratio ν in each difference map $\mathbf{x}_d = \mathbf{x}_a - r\mathbf{x}_b$, where a and b denote the two maps (*e.g.*, Ka1/2). When $r = 1$, the sky signal is subtracted completely and ν should be a minimum. On the other hand, with $r \ll 1$ ($r \gg 1$), map a (map b) dominates and ν gives the significance of the anisotropy detection in this map. Figure 5 shows this comparison for all three map pairs and illustrates that despite the substantial signal (which is detected at the significance level of 3σ , 2σ , 1σ , 6σ , 13σ and 20σ in the Ka1, Ka2, Q1, Q2, Q3 and Q4 channels, respectively), none of the difference maps show any significant remaining structure. Q3 and Q4 are particularly significant since they are the only maps to cover the big cold spot seen in Figure 3 and in the Saskatoon data (Netterfield et al. 1997). The spectral analysis of the data will be presented in a future paper.

5. CONCLUSIONS

The second flight of QMAP produced a map of the sky covering 83 square degrees at resolutions of $0^{\circ}.7$ – $0^{\circ}.9$ and frequencies of 42–31 GHz with $\gtrsim 20\sigma$ detection of anisotropy. Systematic checks strongly suggest that this

anisotropy is on the sky rather than produced by the instrument. We also present an angular power spectrum covering $40 < \ell < 200$ produced from the map. In this region of the sky, the CMB is the dominant source of anisotropy at 30–40 GHz (de Oliveira-Costa et al. 1997); thus we interpret the observed signal as predominantly CMB anisotropy. The raw data will be made public upon publication of this *Letter*.

Table 1. — Flight 2 Angular Power Spectrum. The band powers $\delta T_\ell = [\ell(\ell+1)C_\ell/2\pi]^{1/2}$ have window functions whose mean and rms width are given by ℓ_{eff} and $\Delta\ell$. The errors δT include both noise and sample variance, and are uncorrelated for the two Ka-points.

Band	ℓ_{eff}	$\Delta\ell$	δT [μK]
Ka	91	47	46^{+10}_{-12}
Ka	145	64	63^{+10}_{-12}
Q	125	67	56^{+5}_{-6}

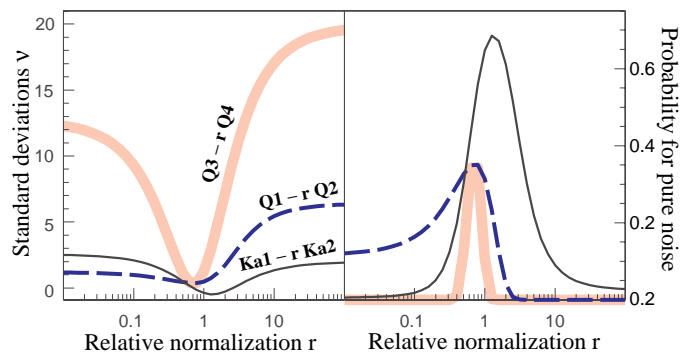


FIG. 5.— Evidence for real sky signal in the maps. The left panel shows the signal-to-noise ratio ν in difference maps weighted by r (see text) for Ka1 vs. Ka2 (solid black), Q1 vs. Q2 (dashed) and Q3 vs. Q4 (grey). The right panel shows the corresponding probability that the difference map contains noise only. This figure shows that all maps except Q1 contain significant detection of anisotropy and that the signal is common to both maps of each polarization pair.

We are grateful for the invaluable support of the NSBF and we thank Eric Torbet for his contributions. This work was supported by a David & Lucile Packard Foundation Fellowship (to LP), a Cottrell Award from Research Corporation, an NSF NYI award, NSF grants PHY-9222952 and PHY-9600015, NASA grant NAG5-6034 and Hubble Fellowships HF-01044.01–93A (to TH) and HF-01084.01–96A (to MT) from by STScI, operated by AURA, Inc. under NASA contract NAS5-26555.

REFERENCES

- Baars, J. W. M., Genzel, R., Pauliny-Toth, I. I. K., & Witzel, A. 1977, *A&A*, 61, 99
- Chini, R., Kreysa, E., Mezger, P. G., & Gemünd, H.-P. 1984, *A&A*, 137, 117
- de Oliveira-Costa, A., Kogut, A., Devlin, M. J., Netterfield, C. B., Page, L., & Wollack, E. J. 1997, *ApJ*, 482, L17
- de Oliveira-Costa, A., Devlin, M. J., Herbig, T., Miller, A. D., Netterfield, C. B., Page, L., & Tegmark, M. 1998, *astro-ph/9808045* (dO98)
- Devlin, M. J., de Oliveira-Costa, A., Herbig, T., Miller, A. D., Netterfield, C. B., Page, L., & Tegmark, M. 1998, *astro-ph/9808043* (D98)
- Leitch, E. M. 1998, Ph.D. Thesis, California Institute of Technology
- Mezger, P. G., Tuffs, R. J., Chini, R., Kreysa, E., & Gemünd, H.-P. 1986, *A&A*, 167, 145
- Netterfield, C. B., Devlin, M. J., Jarosik, N., Page, L., & Wollack, E. J. 1997, *ApJ*, 474, 47
- Tegmark, M. 1996, *Phys. Rev. D*, 55, 5895
- Wollack, E. J., Devlin, M. J., Jarosik, N., Netterfield, C. B., Page, L., & Wilkinson, D. 1997, *ApJ*, 476, 440